Ultrathin Lateral 2D Photodetectors using Transition Metal Dichalcogenides $PtSe_2$-WS_2-$PtSe_2$ by Direct Laser Patterning

Linlin Hou[1], Wenshuo Xu[2], Qianyang Zhang[1], Viktoryia Shautsova[1], Jun Chen[1], Yu Shu[1], Xuan Li[1], Harish Bhaskaran[1] and Jamie H. Warner[3,4]*

[1] Department of Materials, University of Oxford, Parks Road, Oxford, OX1 3PH, United Kingdom

[2] Department of Physics, National University of Singapore, 2Science Drive 3, 117551, Singapore

[3] Materials Graduate Program, Texas Materials Institute, The University of Texas at Austin, 204 East Dean Keeton Street, Austin, Texas 78712, United States

[4] Walker Department of Mechanical Engineering, The University of Texas at Austin, 204 East Dean Keeton Street, Austin, Texas 78712, United States

* jamie.warner@austin.utexas.edu

Abstract

Layer-dependent band structure evolution of transition metal dichalcogenides (TMDs) endows them with various bandgap from insulating to semiconducting to conductive. Here we demonstrate a metal-semiconductor-metal (MSM) photodetector using only TMDs materials

for both electrodes and photoactive materials. Semimetal few-layered $PtSe_2$ acts as metal electrodes and monolayer WS_2 acts as photoactive material. $PtSe_2$ was synthesized by thermally assisted selenization and the device was fabricated by using photolithography coupled with direct laser patterning. By modifying the scanning step during the laser patterning process, various channel width can be achieved. As-fabricated devices exhibit satisfactory ON/OFF ratio and fair photoresponse. Comparison study shows that device with shorter channel width have better photoresponsivity. Back-to-back Schottky diodes model well estimates the barrier height of $PtSe_2/WS_2$ heterojunction. The device also exhibits the lowering of barrier height with increasing laser power, owing to the photogating effect. Our study widens the material choices for 2D electrodes and investigates the feasibility of the low-cost laser patterning on the fabrication of optoelectronic devices.

Keywords: laser patterning, device fabrication, two-dimensional materials, transition-metal dichalcogenides, $PtSe_2$, WS_2, Schottky barrier lowering, photodetector

Introduction

Layered materials beyond graphene have attracted people's attention for few years due to their unique optical and electrical properties derived from quantum confinement effect, which makes them promising candidates for ultrathin and flexible next-generation photonics and electronics.[1,2] Transition metal dichalcogenides (TMDs) is a class of layered materials in a form of MX_2, where M and X represent a transition metal atom (group 4-10) and a chalcogen atom respectively.[3] Transition metal atoms are covalently bonded with adjacent chalcogen atoms to form a sandwiched structure. TMDs layer are weakly stacked together via van der Waals (vdW) interaction to form their bulk counterparts. One of the most fascinating properties of TMDs is that their band structure evolved with their thickness. On the one hand, for group 4 TMDs, such as molybdenum disulphide (MoS_2) and tungsten disulphide (WS_2), they have been extensively studied for their strong light matter interactions due to their indirect-to-direct

bandgap transition when thinning down to monolayer.[4–7] Thereby, monolayer group 4 TMDs are widely used as photoactive materials in applications of opto-electronics, such as photodetector, LED and photovoltaic device.[8–12] On the other hand, for group 10 TMDs, exemplified by noble metal TMDs $PtSe_2$, the energy bandgap narrows down from 1.38 eV to negative band gap when the thickness increasing from monolayer to its bulk counterpart.[13–15] Accordingly, monolayer $PtSe_2$ is considered as semiconductor while bulk $PtSe_2$ thin film can be defined as semimetal.[14] Semiconducting monolayer $PtSe_2$ shows high mobility and good air-stability, rendering it promising in the field of photocatalysis, sensing and opto-electronics.[16–19] However, the semimetal behaviour of $PtSe_2$ bulk material is rarely mentioned, which provides another choice of 2D materials beyond graphene serving as metal contacts in electronic devices.

Similar with the synthesis of group 4 TMDs materials, which has been widely explored, there are two basic strategies to synthesize $PtSe_2$: top-down route (peel off single- or few-layered materials from their corresponding bulk crystals) and bottom-up route (direct growth of materials from molecular level on substrates).[20] Mechanical exfoliation,[21,22] one of the most widely used top-down methods, can obtain defect free $PtSe_2$ crystal but has limitations in scale-up and uncontrollable shape for following industrial applications. Chemical vapour deposition (CVD)[23], chemical vapour transport (CVT)[24], and molecular-beam epitaxy (MBE)[25] can also produce high quality monolayer $PtSe_2$ but require high growth temperature and low vacuum. Thermally assisted selenization[18,26] and plasma-assisted selenization[27] are able to synthesize $PtSe_2$ thin film from monolayer to bulk at lower temperature (usually < 400 ^oC), which can be used in applications with less strict requirement for crystal quality.

Direct laser patterning is a more approachable, less time-consuming and low-cost technique. For traditional metals, electron-beam lithograohy (EBL) is a high-cost technique to make channels for electrodes within a range from hundreds nm to few μm, yet with great

necessity. Recent discussions on laser thinning technique using on tailoring TMDs have been made, [28–31] which opens up a way to apply laser patterning on TMDs-based device fabrication. For example, $PdSe_2$ thin film can be ablated by using controlled laser ablation.[28] Comparing with graphene electrode, $PtSe_2$ electrode can greatly reduce the contact resistance in $PtSe_2$ homojunction.[32] Therefore, the exploration of making $PtSe_2$ electrode using low-cost technique is of significant importance for future opto-electronic device fabrication.

Here, we demonstrate a lateral structural of $PtSe_2$-WS_2-$PtSe_2$, where few-layered $PtSe_2$ thin film works as metal electrodes and monolayer WS_2 acts as photoactive material. We fabricated the device using direct laser patterning and investigated the relevant optoelectronic properties of the device, where $PtSe_2$ thin film was synthesized by thermally assisted selenization. Such lateral structure can be considered as a metal-semiconductor-metal (MSM) configuration, which is a typical configuration for photodetector applications.[8,33,34]

Results and discussion:

$PtSe_2$ was synthesized by a simple epitaxial method: pre-deposition of platinum (Pt) layer followed by a direct selenization process in ambient pressure. Figure 1 a) schematically illustrated the growth of few-layered $PtSe_2$ thin film. 2 nm platinum was firstly deposited on a silicon substrate (SiO_2/Si, with 300 nm thickness SiO_2) by electron-beam evaporation. The silicon substrate with pre-deposited Pt layer shows a mirror-like silver surface. A double-furnace system was utilised for the following selenization process. Selenium (Se) powder was placed in the centre of furnace 1 while silicon wafer with uniformly coated Pt was situated in the centre of furnace 2. Furnace 1 and furnace 2 were ramped up to and stabilized at 230 ^oC and 350^oC respectively. Pure argon (Ar) was used to flush the system and carry with the Se vapour downstream to the substrate. The whole selenization process lasted for 40 min to form the $PtSe_2$ thin film. The as-synthesized $PtSe_2$ film shows an mirror-like surface analogous to

Pt layer. The atomic model in Figure 1 b) shows the selenization process of Pt substrate. Figure 1 c) shows the SEM image of as-synthesized $PtSe_2$ thin film. SEM image demonstrates a fairly smooth surface with very few Se precursor accumulated on it. Figure 1 d-e) shows the TEM image of $PtSe_2$ thin film and its corresponding fast Fourier transform (FFT) image. The FFT image shows that the d spacing of (100) crystallographic planes is 3.2 Å. Both TEM image and FFT image demonstrate that the $PtSe_2$ has a hexagonal lattice, with an lattice constant a = 3.7 Å, which is consistent with the theoretical value of $PtSe_2$.[35] Figure 1 f) shows the Raman spectrum of $PtSe_2$ film. Two predominant characteristic peaks at 176.7 cm^{-1} and 205.7 cm^{-1} represent the in-plane vibration (E_g) of Se atoms in opposite direction and out-of-plane vibration (A_{1g}) of Se atom respectively. A broad but less pronounced peak at 229.7 cm^{-1} can be interpreted as an superposition of two longitudinal optical (LO) mode of E_u and A_{2u}, depicting the in-plane and out-of-plane of Pt and Se atoms respectively. These features in the Raman spectrum of as-synthesized $PtSe_2$ thin film are in accordance with the reported few-layered $PtSe_2$ samples synthesized by direct selenization of Pt.[24,36,37] The inset of Figure 1 g) shows the AFM image of the $PtSe_2$ film, where the sharp edge comes from the scratch by a tungsten probe tip (SEM image of this aera is shown in Figure S1). Figure 1 g) describes the height profile of line 1 drawn in AFM images. The step height can be estimated as 11.2 nm, implying the $PtSe_2$ thin film is few-layered. The results of energy dispersion X-ray spectroscopy (EDS) which has been done on a TEM grid, as shown in figure 1 h), also proves the successful growth of few layered $PtSe_2$ thin film.[21]

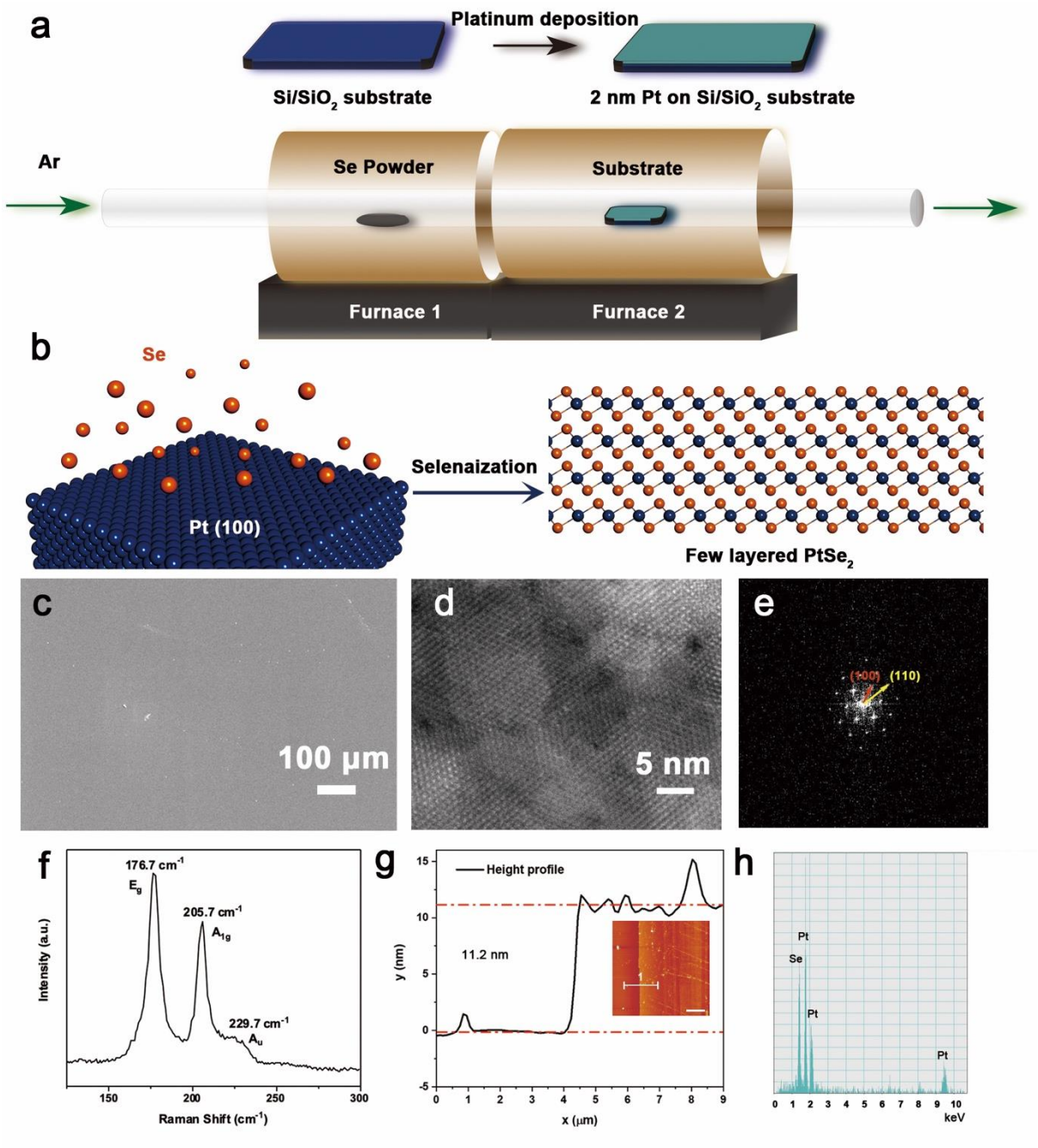

Figure 1. Synthesis of $PtSe_2$ thin film. a) Experimental setup for synthesis of $PtSe_2$ thin film: direct selenization of a pre-deposited platinum layer on the silicon substrate. b) Atomic model of selenization of few-layered $PtSe_2$. c) SEM image of as-synthesized $PtSe_2$ thin film. d) TEM of as-synthesized $PtSe_2$ thin film. e) Corresponding FFT image of d). f) Raman spectrum of as-synthesized $PtSe_2$ thin film. g) Height profile for as-synthesized $PtSe_2$ thin film (inset: AFM image with a scanned line labelled as 1). h) EDS spectrum of as-synthesized $PtSe_2$ thin film.

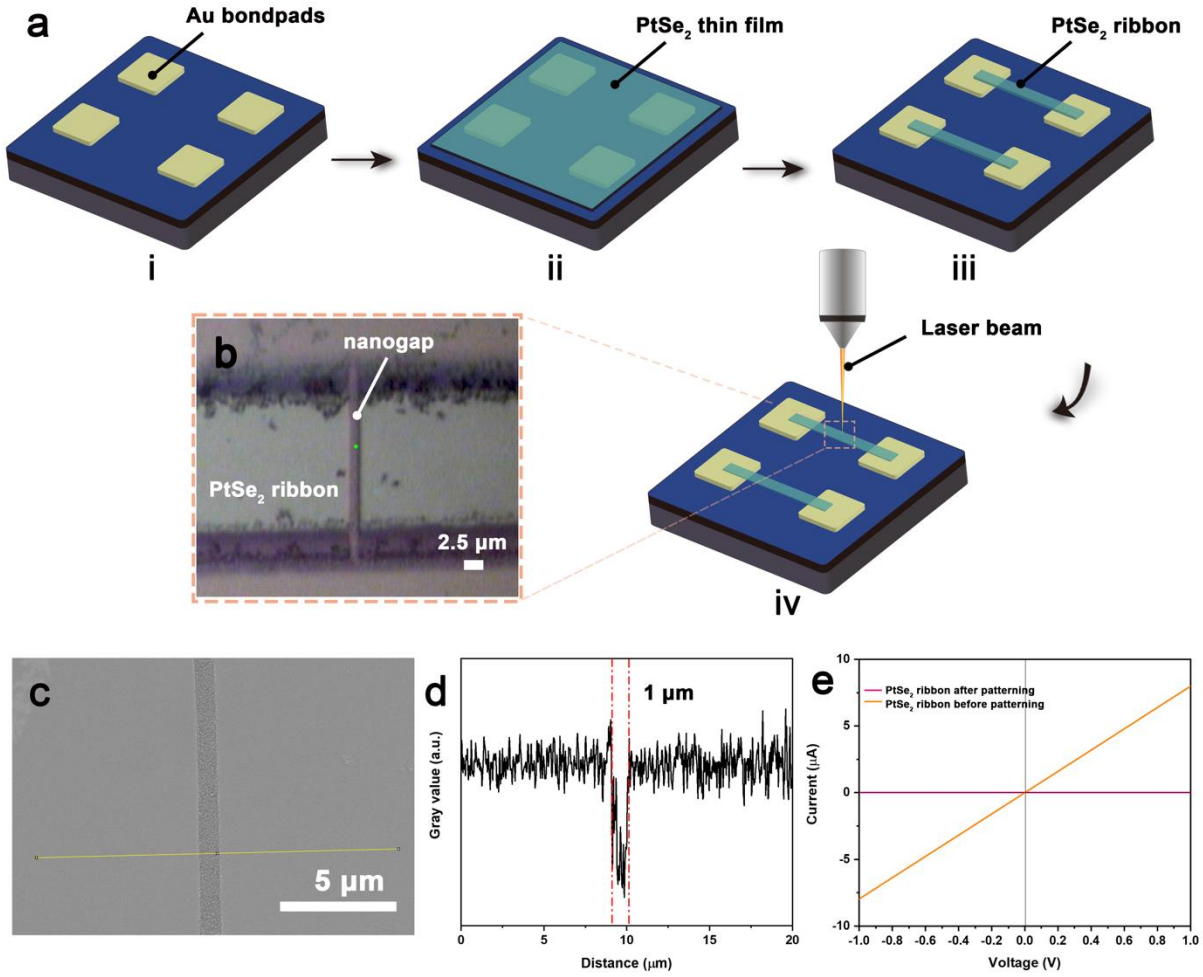

Figure 2. Fabrication process of $PtSe_2$ contacts. a) Schematical illustration for fabrication process of $PtSe_2$ ribbons with nanogap: i) deposit gold bond pads on silicon substrate; ii) transfer $PtSe_2$ thin film to silicon substrate; iii) pattern $PtSe_2$ ribbons by photolithography; iv) pattern nanogap on $PtSe_2$ ribbon by direct laser patterning. b) Optical image of a typical $PtSe_2$ ribbon with nanogap. c-d) Width measurement for channel with a scanning step of 200 nm: c) SEM image, d) corresponding gray value profile of the yellow line drawn in c). e) I-V curves of the $PtSe_2$ ribbon and $PtSe_2$ ribbon before and after laser patterning.

Figure 2 a) schematically illustrates the step-by-step fabrication process of $PtSe_2$ contact. Cr/Au (5 nm/60 nm) bond pads (150×150 μm^2) were firstly patterned and deposited on the silicon substrate by using electron-beam lithography (EBL) and thermal evaporation. $PtSe_2$ thin film was then transferred onto the silicon substrate with gold bond pads by using a

water-based wet transfer. Both the thickness of $PtSe_2$ thin film and the mass of Pt and Se elements determine that a long time is needed to etch the unwanted area by oxygen plasma, suggesting that a thicker resist is required. Considering that the resists for EBL is relatively thin due to the limitation of the free path of electrons, photolithography was employed here to pattern $PtSe_2$ ribbons right above the Au bond pad, since a much thicker photoresist can be obtained. S1813 is a positive photoresist with larger resistance for oxygen plasma, which is able to achieve a thickness in few microns by adjusting the spinning speed. Although S1813 is an ideal photoresist for ribbon patterning, it is notable that a buffering layer of PMMA 495 A4 (with a thickness of 190 nm) is necessary here. This bilayer recipe PMMA/S1813 can not only get rid of the reaction between $PtSe_2$ and MF-319 developer, but also achieve a much cleaner surface. Comparison study of single-layer recipe and bilayer recipe is shown in Figure S2 and Figure S3. Laser patterning was chosen for patterning nanogaps on $PtSe_2$ ribbons, after ruling out EBL for its thin resist layer and photolithography for its resolution owing to the diffraction limit and the distance between the mask and the sample. During the laser patterning, $PtSe_2$ ribbon was laterally lying under the 100× objective lens to reach a maximum laser power of 7.8 mW while the laser was moving perpendicularly to cut the ribbon along the pre-drawn line. Figure 2 b) shows the optical image of $PtSe_2$ ribbon with a laser-patterned nanogap. The SEM image shown in Figure 2 c) is the $PtSe_2$ ribbons with a nanogap patterned by using a scanning step size of 200 nm during the patterning process. The corresponding gray value profile of the line drawn on SEM image shows that the channel width can be estimated as 1 μm, as shown in Figure 2 c-d). By modifying the scanning step size of the laser beam, we can achieve nanogaps with different width. Figure S4 shows a channel width of 1.5 μm by using a scanning step size of 300 nm. The I-V curves in Figure 1 e) present the conductivity of the $PtSe_2$ ribbon and $PtSe_2$ ribbon with nanogap. The conductivity of the $PtSe_2$ ribbon is calculated as $1.16 \times 10^3\ S/m$ and that of the $PtSe_2$ ribbon with nanogap declines to zero. The SEM images from Figure 2 c)

and Figure S4 a) demonstrate that the oxidised materials left in the region of the gap after laser ablation are particles rather than continuous film. The full scale I-V curve of the patterned ribbon shown in Figure S4 c) that exhibits no output current but only noise levels, can also demonstrates that the $PtSe_2$ material on the channel was fully removed.

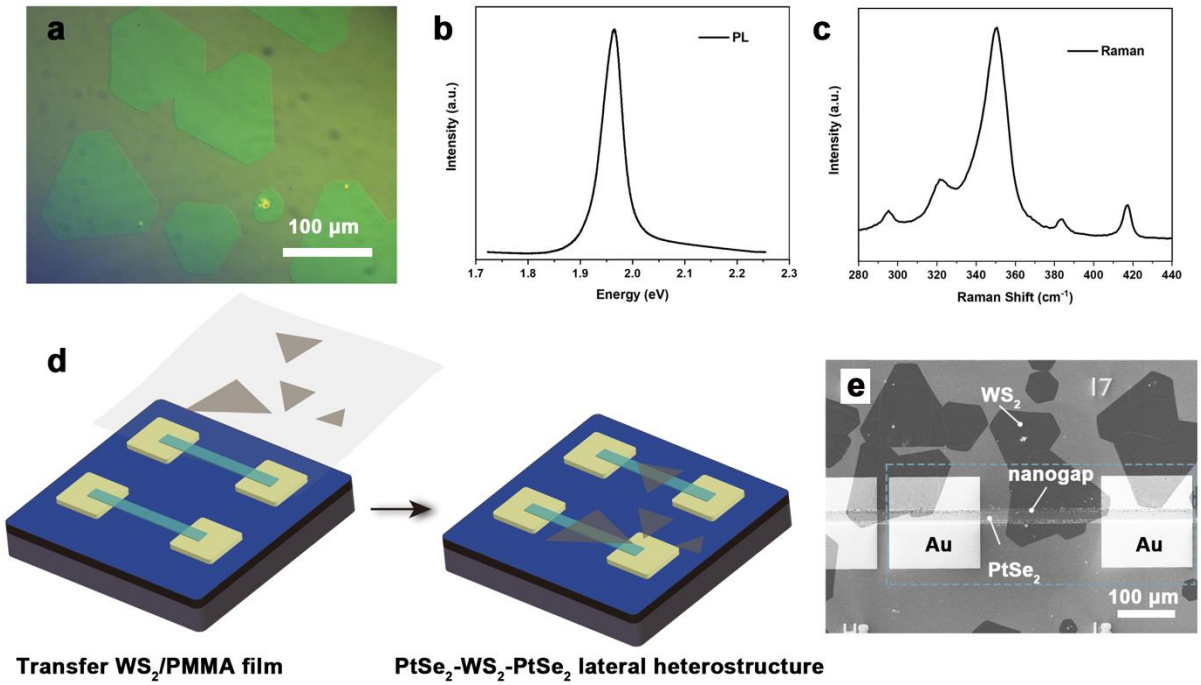

Figure 3. a) Optical images of CVD grown WS_2 single domains. The average grain size can be estimated as 100-150 μm. b-c) PL and Raman spectra of CVD grown WS_2. d) Transfer of WS_2 single domains to $PtSe_2$ contacts. e) SEM image of a typical device with the lateral structure of $PtSe_2$-WS_2-$PtSe_2$.

WS_2 was synthesized by using atmospheric pressure chemical vapour deposition (APCVD), which has been reported in our previous work.[38] Figure 3 a) shows CVD grown WS_2 single domains, with an average domain size from 100 to 150 μm. Figure 3 b-c) shows the photoluminescence (PL) and Raman spectra of as-grown WS_2, in accordance with single layered WS_2 reported.[39] To fabricate the lateral structure of $PtSe_2$-WS_2-$PtSe_2$, the last step is to cover the channel by WS_2 single domains, which was accomplished by aligned transfer to guarantee the success rate of device fabrication, as shown in Figure 3 d).[40] Figure 3 e) shows the SEM image of an as-fabricated device with the lateral structure of $PtSe_2$-WS_2-$PtSe_2$.

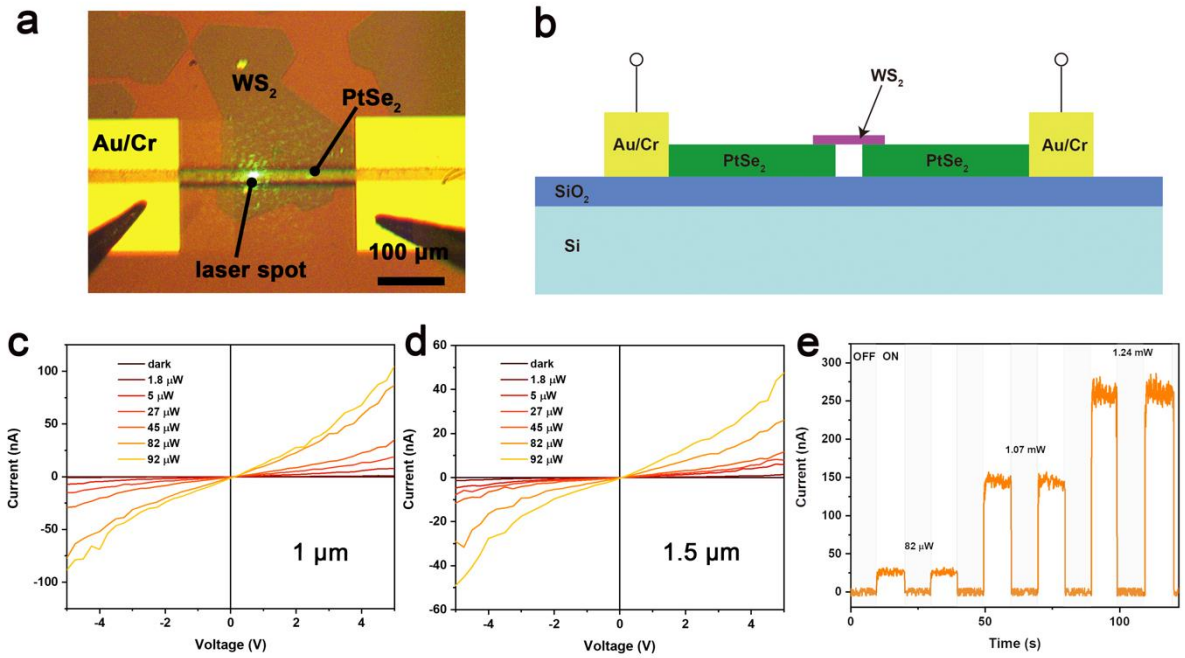

Figure 4. Optoelectrical measurements for $PtSe_2$-WS_2-$PtSe_2$ photodetector. a) Optical image of a typical $PtSe_2$-WS_2-$PtSe_2$ lateral heterostructure under illumination. b) The schematic of the side view for a device under operation. c-d). I-V curves of photodetectors with different channel width (1 μm and 1.5 μm) under different illumination conditions. e) ON/OFF tests for photodetector with a channel width of 1 μm under the bias of +3 V and laser power of 82 μW, 1.07 mW and 1.24 mW. The ON/OFF ratios are 155, 822 and 1438 respectively.

Figure 4 a-b) show the optical image and the side view schematic of a typical $PtSe_2$-WS_2-$PtSe_2$ device under operation. During the device measurements, two tungsten tips were lowered down to get in touch with the gold bond pads, thereby the current flows directly through the lateral stack of $PtSe_2$-WS_2-$PtSe_2$. To prevent the WS_2 from degradation under high bias, we set up our measurements in a range of -5V to +5 V. The output curves for devices with a channel length of 1 μm and 1.5 μm under different illumination condition from the green laser ($\lambda = 532\ nm$) were investigated and shown in Figure 4 c-d). More specifically, Figure S5 shows the I-V curve under dark condition for photodetector with a channel width of 1 μm. Both devices exhibit obvious photoresponse and non-linear I-V curves, which indicates the

Schottky contact at the interface of $PtSe_2$-WS_2 interface. Figure 4 e) shows the time-resolved photoresponse for device with the channel length of 1 μm, under the laser power of 82 μW, 1.07 mW and 1.24 mW, and applied bias of +3 V. The ON/OFF cycles were operated with a time interval of 10 sec. Our device shows a remarkable ON/OFF ratio (I_{ON}/I_{OFF}) (155, 822 and 1438 respectively), good reproducibility, and short response time, (as shown in Figure S6) which make the device a good candidate for photodetector with highly sensible switch.

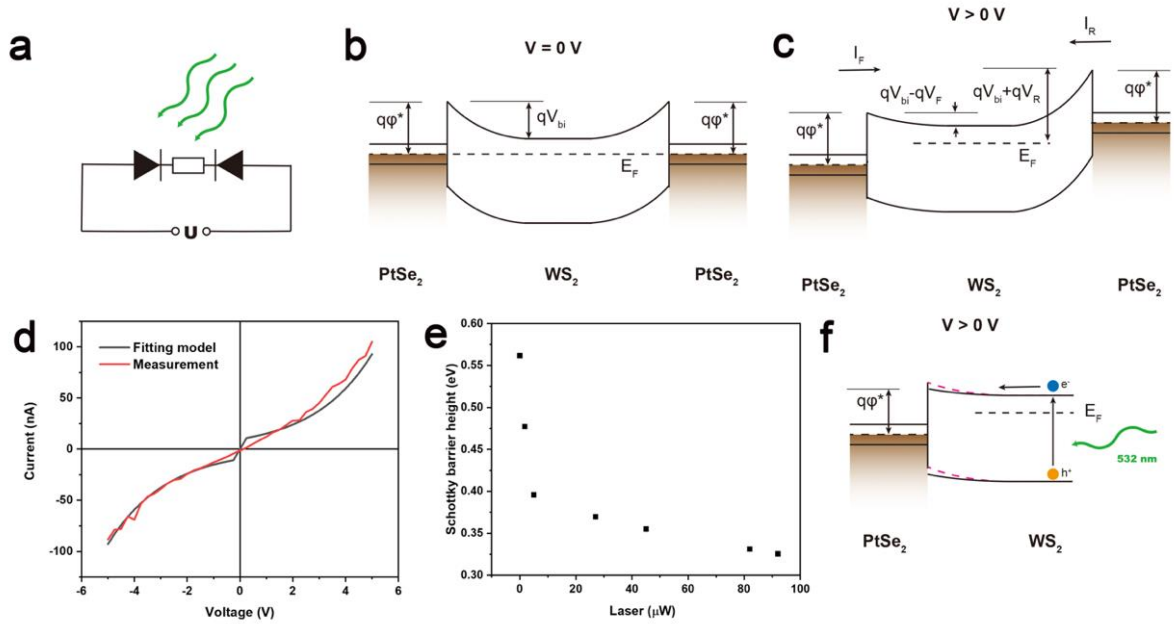

Figure 5. Calculation of Schottky barrier height of $PtSe_2$-WS_2 heterojunction. a) Equivalent circuit diagram of the back-to-back Schottky diodes model. b-c) Band diagrams for Schottky barriers on both sides of $PtSe_2$-WS_2-$PtSe_2$ heterojunction without bias and with positive bias. d) Curve fitting of the I-V curve of $PtSe_2$-WS_2-$PtSe_2$ film by using back-to-back Schottky diodes model. e) Calculated Schottky barrier height as a function of incident laser power. f) Band diagram for $PtSe_2$-WS_2 heterojunction under illumination. The pink dashed lines exhibit the conduction band and valance band of WS_2 under dark condition.

We then further investigate the mechanism of photoresponse for the $PtSe_2$-WS_2-$PtSe_2$ lateral device. As we mentioned before, the non-line I-V curves imply that $PtSe_2$-WS_2 heterojunction can be considered as a Schottky contact. In this way, the $PtSe_2$-WS_2-$PtSe_2$ lateral heterostructure can be regarded as a Metal-Semiconductor-Metal (MSM) photodetector.

A simplified back-to-back Schottky diodes model was used here to describe the $PtSe_2$-WS_2-$PtSe_2$ lateral heterostructure, as shown in Figure 5 a), where two $PtSe_2$-WS_2 Schottky diodes and a WS_2 resistor are series connected to form an electrical circuit. Figure 5 b-c) schematically illustrate the band diagrams of the lateral structure with and without bias. In idea condition without bias, we assume that the gap distance between $PtSe_2$ and WS_2 is in atomic scale and transparent to electrons when $PtSe_2$ electrodes get in contact with WS_2 and establish a single system in thermal equilibrium. V_{bi} is the built in electrical field within the depletion layer in WS_2 induced by the negative charges accumulated in metal surface and positive charge existed in WS_2 surface, as shown in Figure 5 b). The positive bias applied to the system is a forward bias for one $PtSe_2$-WS_2 diode and a reversed bias for the other one due to the intrinsic nature of the diode, as illustrated in Figure 5 c). The current of the circuit is dominated by diode under reversed bias in low bias regime and that under forward bias in high bias regime. I-V curves in Figure 4 c) were fitted by using back-to-back diodes model (Supporting Information S6). Figure 5 d) is an example of curve fitting by using back-to-back Schottky diodes model, suggesting that the model well fits the I-V curve we measured. We extracted the ϕ^* of the $PtSe_2$-WS_2 heterojunction at each illumination condition and plotted them in Figure 5 d). The work function of multilayer PtSe2 (ϕ_{PtSe_2}) is 4.76 eV and the electron affinity of WS_2 (χ_{WS_2}) is 4.0 eV.[41] In ideal condition, the Schottky barrier (ϕ_{SB}) is supposed to be $\phi_{SB} = \phi_{PtSe_2} - \chi_{WS_2} = 0.76\ eV$ according to Schottky-Mott rule. However, the calculated effective Schottky barrier height is 0.56 eV in dark condition. This overestimation of Schottky barrier height by Schottky-Mott rule is mainly due to the interface states situated on WS_2. These trapped states caused Fermi-pinning effect at the WS_2 interface, leading to a lower effective Schottky barrier height. Another finding we noticed from Figure 5 e) is that the effective Schottky barrier height is decreasing with increasing laser power. The lowering of Schottky barrier height can be explained by increasing of photoinduced trapped states concentration. As shown in Figure 5 f),

under the illumination of incident light, generated electron-hole pairs are separated to conductive band and valence band respectively. Electrons on conductive band migrate to $PtSe_2$ electrode while holes on valance band are drifting to the interface of WS_2 and trapped at the surface. Such increasing interface states concentration leads to accumulation of positive charge at the interface of WS_2, which lowers the local Fermi level of WS_2 and further the reduce the effective Schottky barrier height. Here, carriers in trapped states function as local gates and modulate the barrier height. Analogous photogating/photo induced lowering of Schottky barrier height has been reported on Au-WS_2, graphene-MoS_2 surface.[33,42]

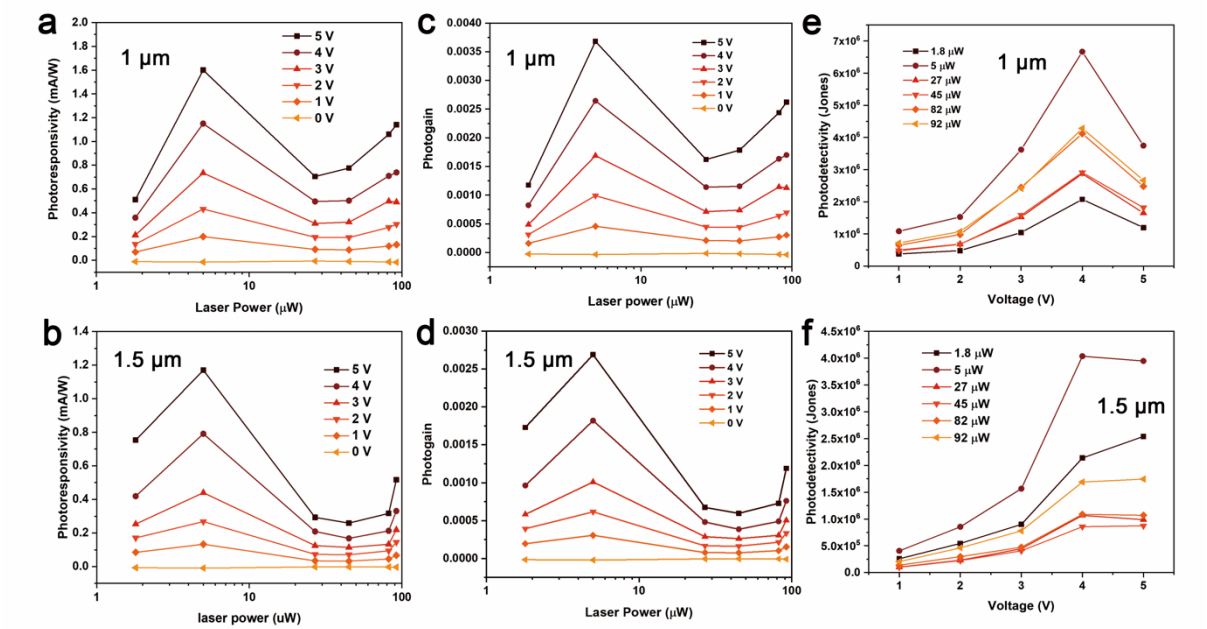

Figure 6. a-b) Photoresponsivity and c-d) Photogain of photodetectors with a channel width of 1 μm and 1.5 μm as a function of incident laser power. e-f) Specific detectivity of two types of photodetector as a function of applied bias.

Photoresponsivity, photogain and photodetectivity are three significant quantity of interest for the performance of a photodetector. Photoresponsivity (R) is a directly measurement of the current generated by the incident light:

$$R = \frac{I_{photo}}{P_{light}}$$

where I_{photo} is photocurrent generated under certain illumination condition and P_{light} is the illumination power. Figure 6 a-b) show the calculated photoresponsivity of devices with different channel length as a function of laser power under certain applied bias. As we can see, photoresponsivity is increasing with increasing bias. The maximum R for devices with channel length of 1 μm and 1.5 um are 1.6 mA/W and 1.2 mA/W respectively, both of them were measured under the maximum applied bias of 5V and laser power of 5 μW. As we can see, the relationship of the responsivity and laser power is not simply monotonic. In low illumination condition, the increase of R comes from the drastically decrease of Schottky barrier height induced by photogating effect, as shown in Figure 5 d) (1.8 μW and 5 μW). Afterwards, when photogating effect gradually reaches a relatively steady state value, the trapped states are fully filled and changes in Schottky barrier height is very little. When the system reaches the saturation, more illumination would not give higher current, the R starts to drop. However, with continuously increasing laser power, the photovoltaic signal starts to emerge from the noise levels and contribute to the photocurrent, which is attributed to the re-growth of the photoresponsivity at the end of high powers. Photogain (G) measures the degree of multiplication,[43] caused by different charge mobility of electrons and holes. Accordingly, external photogain (G_{ext}) is defined as the ratio of the number of electron circulated in the circuit to the number of incident photons:

$$G_{ext} = \frac{N_{electron\ circulated}}{N_{incident\ photon}} = \frac{I_{photo}/e}{P_{light}/hv} = \left(\frac{hv}{e}\right) R$$

where e is elemental charge, h is Planck's constant, and v is the frenquency of incident light. From the equation above, we can see that the G_{ext} is proportional to R, which is also confirmed in the plots in Figure 6 c-d). The highest G_{ext} for both type of devices were also under the maximum applied bias of 5V and laser power of 5 μW, with a value of 0.0037 and 0.0027 for channel length of 1 μm and 1.5 μm respectively. In the calculation of photogain, there is an

hidden assumption that all of the incident light was fully absorbed and transferred to generate charge carriers. To modify the calculated results, we take the absorbance of WS_2 (8%) into consideration, and the recalculated photogain is 0.046 and 0.033 for devices with the channel length of 1 μm and 1.5 μm. Photogain is largely dependent on the lifetime of the hole ($\tau_{lifetime}$) and the electron transit time ($\tau_{transit}$), as photogain can be expressed as $G = \frac{\tau_{lifetime}}{\tau_{transit}}$. The relatively long channel length leads to a large electron transit time, which is the dominant reason for small gain. The Specific detectivity (D^*) is a figure of merit that includes the geometry, noise and bandwidth of the device, and defined as following:

$$D^* = \frac{R(AB)^{\frac{1}{2}}}{i_n}$$

where A is the effective area of the photodetector, B is the electrical bandwidth, i_n is the measured noise current. An assumption can be adopted here for a quicker estimation, which is that the noise of the photocurrent is dominated by shot noise.[34,44] Therefore:

$$D^* = \frac{RA^{\frac{1}{2}}}{(2eI_{dark})^{\frac{1}{2}}}$$

Figure 6 e-f) shows the specific detectivity for both devices under different illumination power and bias. The maximum D^* for devices with a channel length of 1 μm and 1.5 μm are $6.7 \times 10^6\ Jones$ and $4.0 \times 10^6\ Jones$, under the illumination power of 5 μW and applied bias of 4 V. Despite of the high ON/OFF ratio, our devices show limited performance in photoresponsivity, photogain and specific detectivity, comparing with most reported WS_2-based MSM photodetectors (Supporting Information S7). One of the possible reason is the conductivity of the $PtSe_2$ electrodes is relatively small ($1.16 \times 10^3\ S/m$), compared with other metal or graphene electrodes.[42] Another possible reason is that the residues caused by laser ablation and accumulated on the edge of the channel, which increases the contact resistance between $PtSe_2$ and WS_2.[45] For the comparison study of the device with different channel width,

we noticed that device with shorter channel length have better performance on photoresponsity, photogain and specific detectivity. This is because more electron-hole recombination occurs in devices with longer channel width.[33]

Conclusion

In summary, we demonstrated a photodetector with the lateral structure of $PtSe_2$-WS_2-$PtSe_2$, where we used multilayer $PtSe_2$ to substitute traditional metal electrode to form a typical MSM heterostructure. $PtSe_2$ film was synthesized in a double-furnace system under the ambient pressure by direct selenization of a pre-coated Pt layer on the Si substrate. The film is quite homogenous and was estimated as 11 nm. A bilayer photoresist recipe was used to pattern $PtSe_2$ ribbons using photolithography. Direct laser patterning was used to pattern the nanogap on $PtSe_2$ ribbon. By modifying the scanning steps during the laser patterning process, nanogap with different width can be achieved. $PtSe_2$-WS_2-$PtSe_2$ photodetector shows a remarkable I_{ON}/I_{OFF} of 155 under the illumination power of 82 μW. High I_{ON}/I_{OFF}, good reproducibility, and short response time make our device a good candidate for photodetector. However, the device exhibits lower photogain and photoresponsivity than other group 4 TMDs-based MSM photodetector reported, due to the long electron transit time, relatively low conductivity of the $PtSe_2$ electrodes and residues generated by laser ablation. The device with shorter channel length has better performance on the photoresponse, for more electron–hole recombination occurs in devices with longer channel length. Back-to-back Schottky diodes model was applied to estimate the barrier height of $PtSe_2/WS_2$ heterojunction. The barrier height decreases with increasing laser power, which can be explained by photoinduced lowering of Schottky barrier height. For the future work, we can also fabricate a lateral structure of few-layered $PtSe_2$-monolayer $PtSe_2$-few-layered $PtSe_2$ by using direct laser to thin down few-layered $PtSe_2$ film on the channel area to monolayer semiconductor. In this way, the contact resistance at the

interface between few-layered $PtSe_2$ electrode and monolayer $PtSe_2$ semiconductor can be largely reduced, comparing with using graphene electrode. In addition, the thickness of $PtSe_2$ lying on the channel can be easily tuned by parameters during the laser patterning, which is promising for broadband photodetector. Our study provides a new opportunity for the material choices of 2D electrodes and explores the possibility of applying low-cost laser patterning on the fabrication of optoelectronic devices.

Experimental methods

$PtSe_2$ synthesis:

A 2 nm Pt layer was first deposited on top of a SiO_2/Si substrate via e-beam evaporation. Selenium powder (Se, ≥99.5%, Sigma-Aldrich) and the substrate with uniform Pt coating were loaded in a 2 inch-diameter quartz tube. Two individual furnaces were used to control the temperature of Se and Si substrate with Pt coating. Once sealed, the system was first flushed with pure argon (Ar) flow for 30 min to drive off all the reactive gases in air such as oxygen. After that, Se and the substrate were ramped up to 230 and 350 °C respectively, at which point the selenization began. We continued utilizing Ar flow as the carrier gas to transport Se vapour downstream to the substrate surface. This process lasted for 40 min, leading to formation of $PtSe_2$. Finally, the reaction ended by slow-cooling of both the Se and the as-produced $PtSe_2$ with Ar flow.

CVD synthesis of WS_2:

WS_2 single domains were grown on a 2 cm × 2 cm SiO_2/Si substrate in a double furnace system in ambient pressure. Sulfur powder (300 mg, purum grade >99.5%, Sigma-Aldrich) and WO_3 (200 mg, puriss grade >99%, Sigma-Aldrich) were separately placed in outer and inner tube, and two individual furnaces were used to control each temperature. The Si substrate was

situated downstream S and WO_3. The system was firstly flushed with pure Ar for 30 min before the ramping of the temperature to exhaust the air in the system. Ar flow also transport the upstream S and WO_3 vapour to the Si substrate during the material growth. The growth started at the time when S and WO_3 reached to 180 ^oC and 1145 ^oC together. The growth time lasted for 3 min. Finally both furnace was turned off and moved away for fast cooling with Ar flow.

Material transfer:

Poly(methyl methacrylate) (PMMA) (495A8, MicroChem) was firstly spin-coated (4500 rpm for 60 s, 500 nm) to WS_2 or $PtSe_2$ surface and baked at 150 ^oC on hotplate for 90 s. For both WS_2 and $PtSe_2$ were grown on the Si substrate with SiO_2 layer on top, potassium hydroxide (KOH, 1 M, Sigma-Aldrich) were used for etching solution. After thoroughly washed in DI water, the material film covered with PMMA was scooped out to target substrate and naturally evaporated overnight. Finally, PMMA coating was removed in acetone for 4 h after 15 min baking at 150 ^oC on hotplate.

Device fabrication:

A mask aligner for UV photolithography was used to pattern $PtSe_2$ ribbons by using a bilayer resist (PMMA 495 A4/S1813). MF-319 was used as developer and oxygen plasma was used to etch the $PtSe_2$ film to $PtSe_2$ ribbons. LabRam Aramis Raman spectrometer was used for laser patterning, with the laser wavelength of 532 nm and a 100× objective lens. Bond pads were patterned by E-beam lithography (JEOL 5500 FS) and Cr/Au were deposited using a thermal evaporator. PMMA layer was in hot acetone overnight.

Electrical and opto-electronic measurements:

All of the electrical and opto-electronic measurements were performed on a probe station based on a confocal microscope system. The 532 nm diode-pumped solid laser (Thorlabs, DJ523-40) and a 10× objective lens were used to forms a 2 μm spot on the sample. Electrical measurements was carried out by Keithley 2400 source meter.

Supporting Information. AFM study of $PtSe_2$ film; comparison study of single-layer recipe and bilayer recipe for photolithography; channel width measurements; I-V curve for the photodetector under dark condition; time-resolved photoresponse of the device; curve fittings by using back-to-back diodes mode; summarized photoresponsivity of different WS_2-based M-S-M photodetectors

Reference:

(1) Liu, Y.; Weiss, N. O.; Duan, X.; Cheng, H. C.; Huang, Y.; Duan, X. Van Der Waals Heterostructures and Devices. *Nature Reviews Materials*. **2016,** 16042.

(2) Das, S.; Robinson, J. A.; Dubey, M.; Terrones, H.; Terrones, M. Beyond Graphene: Progress in Novel Two-Dimensional Materials and van Der Waals Solids. *Annu. Rev. Mater. Res* **2015**, *45*, 1–27.

(3) Wang, Q. H.; Kalantar-Zadeh, K.; Kis, A.; Coleman, J. N.; Strano, M. S. Electronics and Optoelectronics of Two-Dimensional Transition Metal Dichalcogenides. *Nat. Nanotechnol.* **2012**, *7*, 699–712.

(4) Ovchinnikov, D.; Allain, A.; Huang, Y. S.; Dumcenco, D.; Kis, A. Electrical Transport Properties of Single-Layer WS2. *ACS Nano* **2014**, *8*, 8174–8181.

(5) Splendiani, A.; Sun, L.; Zhang, Y.; Li, T.; Kim, J.; Chim, C. Y.; Galli, G.; Wang, F. Emerging Photoluminescence in Monolayer MoS_2. *Nano Lett.* **2010**, *10*, 1271–1275.

(6) Zhao, W.; Ghorannevis, Z.; Chu, L.; Toh, M.; Kloc, C.; Tan, P.-H.; Eda, G. Evolution of Electronic Structure in Atomically Thin Sheets of WS_2 and WSe_2. *ACS Nano* **2013**, *7*, 791–797.

(7) Gutiérrez, H. R.; Perea-López, N.; Elías, A. L.; Berkdemir, A.; Wang, B.; Lv, R.; López-Urías, F.; Crespi, V. H.; Terrones, H.; Terrones, M. Extraordinary Room-Temperature Photoluminescence in Triangular WS_2 Monolayers. *Nano Lett.* **2013**, *13*, 3447–3454.

(8) Tan, H.; Xu, W.; Sheng, Y.; Lau, C. S.; Fan, Y.; Chen, Q.; Tweedie, M.; Wang, X.; Zhou, Y.; Warner, J. H. Lateral Graphene-Contacted Vertically Stacked WS_2/MoS_2 Hybrid Photodetectors with Large Gain. *Adv. Mater.* **2017**, *29*, 7866-7873.

(9) Zhou, Y.; Tan, H.; Sheng, Y.; Fan, Y.; Xu, W.; Warner, J. H. Utilizing Interlayer Excitons in Bilayer WS2 for Increased Photovoltaic Response in Ultrathin Graphene Vertical Cross-Bar Photodetecting Tunneling Transistors. *ACS Nano* **2018**, *12*, 4669–4677.

(10) Sheng, Y.; Chen, T.; Lu, Y.; Chang, R. J.; Sinha, S.; Warner, J. H. High-Performance WS_2 Monolayer Light-Emitting Tunneling Devices Using 2D Materials Grown by Chemical Vapor Deposition. *ACS Nano* **2019**, *13*, 4530–4537.

(11) Hou, L.; Zhang, Q.; Tweedie, M.; Shautsova, V.; Sheng, Y.; Zhou, Y.; Huang, H.; Chen, T.; Warner, J. H. Photocurrent Direction Control and Increased Photovoltaic Effects in All-2D Ultrathin Vertical Heterostructures Using Asymmetric h-BN Tunneling Barriers. *ACS Appl. Mater. Interfaces* **2019**, *11*, 40274–40282.

(12) Hou, L.; Zhang, Q.; Shautsova, V.; Warner, J. H. Operational Limits and Failure Mechanisms in All-2D van der Waals Vertical Heterostructure Devices with Long-Lived Persistent Electroluminescence. *ACS Nano* **2020**, *14*, 15533-15543.

(13) Zibouche, N.; Kuc, A.; Miró, P.; Heine, T. Noble-Metal Chalcogenide Nanotubes. *Inorganics* **2014**, *2*, 556–564.

(14) Villaos, R. A. B.; Crisostomo, C. P.; Huang, Z. Q.; Huang, S. M.; Padama, A. A. B.; Albao, M. A.; Lin, H.; Chuang, F. C. Thickness Dependent Electronic Properties of Pt Dichalcogenides. *npj 2D Mater. Appl.* **2019**, *3*, 1–8.

(15) Chen, E.; Xu, W.; Chen, J.; Warner, J. H. 2D Layered Noble Metal Dichalcogenides (Pt, Pd, Se, S) for Electronics and Energy Applications. *Mater. Today Adv.* **2020**, *7*, 100076

(16) Singh, A. K.; Mathew, K.; Zhuang, H. L.; Hennig, R. G. Computational Screening of 2D Materials for Photocatalysis. *J. Phys. Chem. Lett.* **2015**, *6*, 1087–1098.

(17) Sajjad, M.; Montes, E.; Singh, N.; Schwingenschlögl, U. Superior Gas Sensing Properties of Monolayer $PtSe_2$. *Adv. Mater. Interfaces* **2017**, *4*, 1600911.

(18) Yim, C.; Lee, K.; McEvoy, N.; O'Brien, M.; Riazimehr, S.; Berner, N. C.; Cullen, C. P.; Kotakoski, J.; Meyer, J. C.; Lemme, M. C.; Duesberg, G. S.. High-Performance Hybrid Electronic Devices from Layered $PtSe_2$ Films Grown at Low Temperature. *ACS Nano* **2016**, *10*, 9550–9558.

(19) Wang, Y.; Yu, Z.; Tong, Y.; Sun, B.; Zhang, Z.; Xu, J. Bin; Sun, X.; Tsang, H. K. High-Speed Infrared Two-Dimensional Platinum Diselenide Photodetectors. *Appl. Phys. Lett.* **2020**, *116*, 211101.

(20) Wang, G.; Wang, Z.; McEvoy, N.; Fan, P.; Blau, W. J. Layered $PtSe_2$ for Sensing, Photonic, and (Opto-) Electronic Applications. *Adv. Mater.* **2021**, *33*, 2004070.

(21) Yu, X.; Yu, P.; Wu, D.; Singh, B.; Zeng, Q.; Lin, H.; Zhou, W.; Lin, J.; Suenaga, K.; Liu, Z.;

Wang, Q. J.. Atomically Thin Noble Metal Dichalcogenide: A Broadband Mid-Infrared Semiconductor. *Nat. Commun.* **2018**, *9*, 1545.

(22) Li, Z.; Zhang, J.; Zeng, Y.; Meng, L.; Zhou, M.; Wu, W. Anomalous Magnetotransport Behaviours in $PtSe_2$ Microflakes. *J. Phys. Condens. Matter* **2017**, *29*, 23LT01.

(23) Wang, Z.; Li, Q.; Besenbacher, F.; Dong, M. Facile Synthesis of Single Crystal PtSe2Nanosheets for Nanoscale Electronics. *Adv. Mater.* **2016**, *28*, 10224–10229.

(24) Zhao, Y.; Qiao, J.; Yu, Z.; Yu, P.; Xu, K.; Lau, S. P.; Zhou, W.; Liu, Z.; Wang, X.; Ji, W.; Chai, Y.. High-Electron-Mobility and Air-Stable 2D Layered $PtSe_2$ FETs. *Adv. Mater.* **2017**, *29*, 1604230.

(25) Yan, M.; Wang, E.; Zhou, X.; Zhang, G.; Zhang, H.; Zhang, K.; Yao, W.; Yang, S.; Wu, S.; Yoshikawa, T.; Miyamoto, K.; Okuda, T.; Wu, Y.; Yu, P.; Duan, W.; Zhou, S.. High Quality Atomically Thin $PtSe_2$ Films Grown by Molecular Beam Epitaxy. *2D Mater.* **2017**, *4*, 045015.

(26) Wang, Y.; Li, L.; Yao, W.; Song, S.; Sun, J. T.; Pan, J.; Ren, X.; Li, C.; Okunishi, E.; Wang, Y. Q.; Wang, E.; Shao, Y.; Zhang, Y. Y.; Yang, H. T.; Schwier, E. F.; Iwasawa, H.; Shimada, K.; Taniguchi, M.; Cheng, Z.; Zhou, S.; Du, S.; Pennycook, S. J.; Pantelides, S. T.; Gao, H. J.. Monolayer $PtSe_2$, a New Semiconducting Transition-Metal-Dichalcogenide, Epitaxially Grown by Direct Selenization of Pt. *Nano Lett.* **2015**, *15*, 4013–4018.

(27) Su, T. Y.; Medina, H.; Chen, Y. Z.; Wang, S. W.; Lee, S. S.; Shih, Y. C.; Chen, C. W.; Kuo, H. C.; Chuang, F. C.; Chueh, Y. L. Phase-Engineered $PtSe_2$-Layered Films by a Plasma-Assisted Selenization Process toward All $PtSe_2$-Based Field Effect Transistor to Highly Sensitive, Flexible, and Wide-Spectrum Photoresponse Photodetectors. *Small* **2018**, *14*, 1800032.

(28) Shautsova, V.; Sinha, S.; Hou, L.; Zhang, Q.; Tweedie, M.; Lu, Y.; Sheng, Y.; Porter, B. F.; Bhaskaran, H.; Warner, J. H. Direct Laser Patterning and Phase Transformation of 2D $PdSe_2$ Films for On-Demand Device Fabrication. *ACS Nano* **2019**, *13*, 14162–14171.

(29) Nagamine, Y.; Sato, J.; Qian, Y.; Inoue, T.; Nakamura, T.; Maruyama, S.; Katsumoto, S.; Haruyama, J. Optoelectronic Properties of Laser-Beam-Patterned Few-Layer Lateral MoS2Schottky Junctions. Appl. Phys. Lett. **2020**, *117*, 043101.

(30) Mine, H.; Kobayashi, A.; Nakamura, T.; Inoue, T.; Pakdel, S.; Marian, D.; Gonzalez-Marin, E.; Maruyama, S.; Katsumoto, S.; Fortunelli, A.; Palacios, J. J.; Haruyama, J.. Laser-Beam-Patterned Topological Insulating States on Thin Semiconducting MoS_2. Phys. Rev. Lett. **2019**, *123*, 146803.

(31) Castellanos-Gomez, A.; Barkelid, M.; Goossens, A. M.; Calado, V. E.; Van Der Zant, H. S. J.; Steele, G. A. Laser-Thinning of MoS_2: On Demand Generation of a Single-Layer Semiconductor. *Nano Lett.* **2012**, *12*, 3187–3192.

(32) Yang, Y.; Jang, S. K.; Choi, H.; Xu, J.; Lee, S. Homogeneous Platinum Diselenide Metal/Semiconductor Coplanar Structure Fabricated by Selective Thickness Control. *Nanoscale* **2019**, *11*, 21068–21073.

(33) Fan, Y.; Zhou, Y.; Wang, X.; Tan, H.; Rong, Y.; Warner, J. H. Photoinduced Schottky Barrier Lowering in 2D Monolayer WS_2 Photodetectors. *Advanced Optical Materials*. **2016**, *4*, 1573–1581.

(34) Tan, H.; Fan, Y.; Zhou, Y.; Chen, Q.; Xu, W.; Warner, J. H. Ultrathin 2D Photodetectors Utilizing Chemical Vapor Deposition Grown WS_2 with Graphene Electrodes. *ACS Nano* **2016**, *10*, 7866–7873.

(35) Jiang, W.; Wang, X.; Chen, Y.; Wu, G.; Ba, K.; Xuan, N.; Sun, Y.; Gong, P.; Bao, J.; Shen, H.; Lin, T.; Meng, X.; Wang, J; Sun, Z.. Large-area High Quality $PtSe_2$ Thin Film with Versatile Polarity. *InfoMat* **2019**, 5, 260–267.

(36) O'Brien, M.; McEvoy, N.; Motta, C.; Zheng, J. Y.; Berner, N. C.; Kotakoski, J.; Elibol, K.; Pennycook, T. J.; Meyer, J. C.; Yim, C.; Abid, M.; Hallam, T.; Donegan, J. F.; Sanvito, S.; Duesberg, G. S.. Raman Characterization of Platinum Diselenide Thin Films. *2D Mater.* **2016**, *3*, 021004.

(37) Lin, S.; Liu, Y.; Hu, Z.; Lu, W.; Mak, C. H.; Zeng, L.; Zhao, J.; Li, Y.; Yan, F.; Tsang, Y. H.; Zhang, X.; Lau, S. P.. Tunable Active Edge Sites in $PtSe_2$ Films towards Hydrogen Evolution Reaction. *Nano Energy* **2017**, *42*, 26–33.

(38) Rong, Y.; Sheng, Y.; Pacios, M.; Wang, X.; He, Z.; Bhaskaran, H.; Warner, J. H. Electroluminescence Dynamics across Grain Boundary Regions of Monolayer Tungsten Disulfide. *ACS Nano* **2016**, *10*, 1093–1100.

(39) Berkdemir, A.; Gutiérrez, H. R.; Botello-Méndez, A. R.; Perea-López, N.; Elías, A. L.; Chia, C. I.; Wang, B.; Crespi, V. H.; López-Urías, F.; Charlier, J. C.;Terrones, H.; Terrones, M.. Identification of Individual and Few Layers of WS_2 Using Raman Spectroscopy. *Sci. Rep.* **2013**, *3*, 01755.

(40) Zhang, Q.; Hou, L.; Lu, Y.; Chen, J.; Zhou, Y.; Shautsova, V.; Warner, J. H. Large-Scale Uniform-Patterned Arrays of Ultrathin All-2D Vertical Stacked Photodetector Devices. ACS Appl. Mater. Interfaces **2021**, *13*, 34696–34704.

(41) Kandemir, A.; Akbali, B.; Kahraman, Z.; Badalov, S. V.; Ozcan, M.; Iyikanat, F.; Sahin, H. Structural, Electronic and Phononic Properties of $PtSe_2$: From Monolayer to Bulk. *Semicond. Sci. Technol.* **2018**, *33*, 085002.

(42) Zhang, W.; Chuu, C.-P.; Huang, J.-K.; Chen, C.-H.; Tsai, M.-L.; Chang, Y.-H.; Liang, C.-T.; Chen, Y.-Z.; Chueh, Y.-L.; He, J.-H.;Chou, M.-Y.; Li, L.-J.. Ultrahigh-Gain Photodetectors Based on Atomically Thin Graphene-MoS2 Heterostructures. *Sci. Rep.* **2015**, *4*, 3826.

(43) Tsai, D. S.; Liu, K. K.; Lien, D. H.; Tsai, M. L.; Kang, C. F.; Lin, C. A.; Li, L. J.; He, J. H. Few-Layer MoS_2 with High Broadband Photogain and Fast Optical Switching for Use in Harsh Environments. *ACS Nano* **2013**, *7*, 3905–3911.

(44) Xie, C.; Mak, C.; Tao, X.; Yan, F. Photodetectors Based on Two-Dimensional Layered Materials Beyond Graphene. *Adv. Funct. Mater.* **2017**, *27*, 1603886.

(45) Račiukaitis, G.; Brikas, M.; Gedvilas, M.; Rakickas, T. Patterning of Indium-Tin Oxide on Glass with Picosecond Lasers. *Appl. Surf. Sci.* **2007**, *253*, 6570–6574.

TOC: